Supporting Information: Enhanced Sorption of Supercritical CO_2 and CH_4 in the Hydrated Interlayer Pores of Smectite

Junyoung Hwang and Ronny Pini*

Department of Chemical Engineering, Imperial College London, SW7 2AZ London, United Kingdom

E-mail: r.pini@imperial.ac.uk

Sample Preparation

The clay mineral samples were ground manually using a mortar and pestle to obtain particles smaller than 50 μm filtered using a mesh. The samples were degassed *ex situ* at 200 °C under continuous vacuum for over 12 h prior to the low-pressure gas (N_2 and Ar) and vapor (H_2O) sorption experiments using Autosorb iQ (Quantachrome Instruments, Florida), and *in situ* at 200 °C under continuous vacuum for over 12 h prior to the high-pressure sorption experiments (He, CO_2, and CH_4) using IsoSORP HPII (Rubotherm, Bochum, Germany). Table S1 summarizes the mass of the samples used for each experiments.

Table S1: Sample mass (in grams) used for the experiments in the study

Instrument	Experiment		STx-1b	SWy-2	ISCz-1	IMt-2
Autosorb iQ	N_2		0.2059	–	–	–
	Ar		0.4408	–	–	–
	H_2O	Run 1	0.1038	0.1130	0.1873	0.1441
		Run 2	0.0963	0.2290	0.1572	0.1569
Rubotherm	He	Dry	1.2722	–	–	2.1296
		Hydrated	0.5522	–	–	1.1168
	CO_2	Dry	1.2655	–	–	2.1299
		Hydrated	0.5792	–	–	0.9936
	CH_4	Dry	1.2700	–	–	2.1303
		Hydrated	0.5846	–	–	0.8057

Experimental Methodology

Low-pressure N_2 and Ar Physisorption

The structural properties of STx-1b, such as its specific surface area, total pore volume, and pore size distribution (PSD), were characterized by the analysis of N_2 (at 77 K) and Ar (at 87 K) physisorption measurements using Autosorb iQ. Figure S1 shows the N_2 and Ar measurements performed in the relative pressure range of 2.0×10^{-6} to 9.9×10^{-1} and 5.5×10^{-6} to 9.9×10^{-1}, respectively.

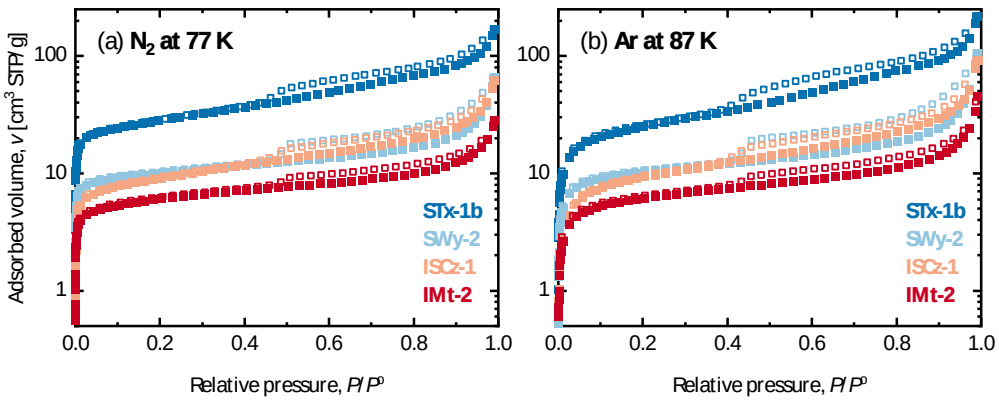

Figure S1: Adsorption (closed symbols) and desorption (open symbols) isotherms of (a) N_2 and (b) Ar on the four clay minerals.

Water Sorption Isotherms

The adsorption and desorption of water was measured using the vapor sorption mode on Autosorb iQ in the relative humidity range of 1.0×10^{-2} to 9.0×10^{-1}. The experiments were repeated at least twice for each clay minerals to confirm the experimental reproducibility as can be in Figure S2.

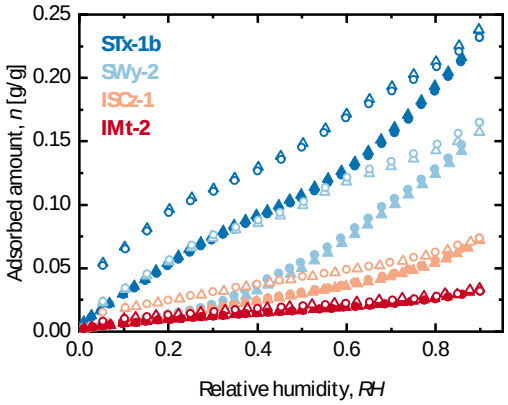

Figure S2: Water adsorption (closed symbols) and desorption (open symbols) isotherms measured using two separate aliquots at 273 K up to 15.8 Torr (RH = 0.9): first runs (triangles) and second runs (circles).

The comparability of the desorption isotherms of STx-1b and SWy-2 shown in Figure S3a demonstrates that the hydration mechanisms are not fully reversible during dehydration, which causes the hysteresis loop of SWy-2 to be larger than that of STx-1b, a common observation between the two montmorillonite samples.[S1–S3] The parallel trend between desorption of STx-1b and SWy-2 indicates that dehydration steps, in which the water adsorbed on the external surface is removed first and the interlayer water remains until low RH due to the relatively strong hydration energy of the cations,[S4] are equally applied to STx-1b and SWy-2. Figure S3b shows that the sorption isotherm of non-swelling IMt-2 resembles the Type II isotherm classified by the recent IUPAC report,[S5] while the sorption isotherm of ISCz-1 is a hybrid of that of SWy-2 (see Figure S2) and IMt-2 showing its mixed layer characteristics.

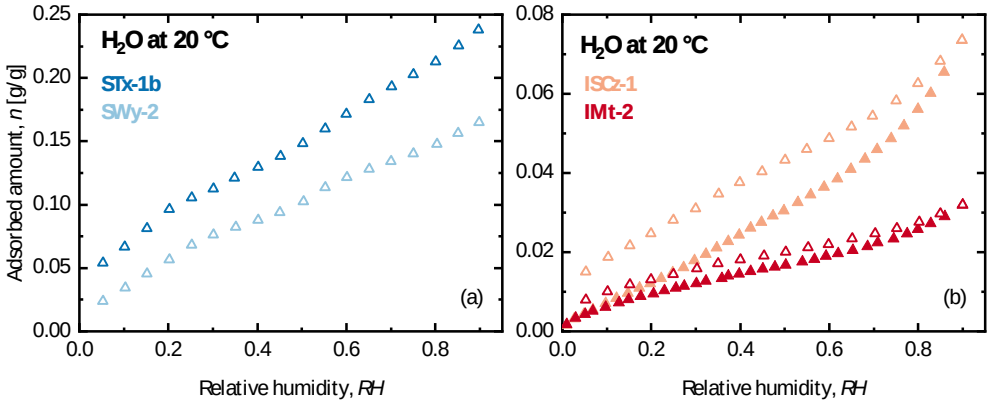

Figure S3: (a) Desorption isotherms of STx-1b and SWy-2 and (b) adsorption (closed symbols) and desorption (open symbols) isotherms of ISCz-1 and IMt-2.

Unconstrained Volumetric Swelling

The extent of swelling of the clay minerals can be inferred from the difference between the total pore volume accessed by adsorbed water and Ar (or N_2) estimated from the sorption isotherms shown in Figure S4. In other words, the extent of volumetric swelling, s, associated

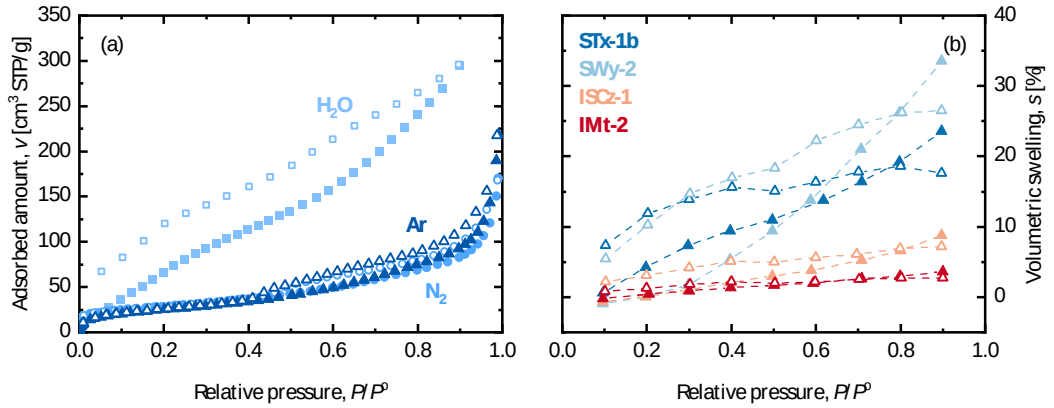

Figure S4: (a) Adsorption (closed symbols) and desorption (open symbols) isotherms of water (293 K), N_2 (77 K), and Ar (87 K) on STx-1b plotted against relative pressure (or humidity). (b) Unconstrained volumetric swelling obtained from the difference between the accessible pore volumes estimated from the adsorption (closed symbols) and desorption (open symbols) isotherms of water and Ar.

with the additional pore volume measured by water can be quantified using the following

equation:

$$s = \rho_{\mathrm{b}}(\tilde{v}_{\mathrm{water}} - \tilde{v}_{\mathrm{g}}) \tag{1}$$

where $\tilde{v}_{\mathrm{water}}$ is the specific pore volume estimated from the adsorbed volume of water at a certain value of RH while $\tilde{v}_{\mathrm{g}}$ is that estimated from the adsorbed gas volume (Ar in this study) at the same value of relative pressure (P/P^{o}). The bulk density, ρ_{b}, is obtained from the following equation:

$$\frac{1}{\rho_{\mathrm{b}}} = v_{\mathrm{g}} + \frac{1}{\rho_{\mathrm{sk}}} \tag{2}$$

where v_{g} is the total specific pore volume estimated by the adsorbed volume of Ar at P/P^{o} of 0.9, and ρ_{sk} is the skeletal density measured by He as discussed earlier. Such swelling can be regarded as unconstrained swelling as net stress is not applied to the clay mineral samples during adsorption measurements.

BET Specific Surface Area

The specific surface areas of the clay minerals were calculated based on the BET theory,[S6] the linearized equation of which is written as follows:

$$\frac{P/P^{\mathrm{o}}}{v\big[1-(P/P^{\mathrm{o}})\big]} = \frac{1}{v_{\mathrm{m}}C} + \frac{C-1}{v_{\mathrm{m}}C}\Big(\frac{P}{P^{\mathrm{o}}}\Big) \tag{3}$$

where v is the amount of adsorbed gas (in cm^3/g STP), v_{m} is the amount of adsorbed gas to form a monolayer on the adsorbent surface, and C is the BET constant. The values of v_{m} and C can be obtained from the slope, s, and the intercept, i, of the linear region when $(P/P^{\mathrm{o}})/\big(v\big[1-(P/P^{\mathrm{o}})\big]\big)$ is plotted against P/P^{o} (RH in the case of water sorption) as can be seen in Figure S5. The BET specific surface area, S_{BET}, is then expressed as:

$$S_{\mathrm{BET}} = \frac{v_{\mathrm{m}}N_{\mathrm{A}}\sigma}{v_{\mathrm{m,STP}}} \tag{4}$$

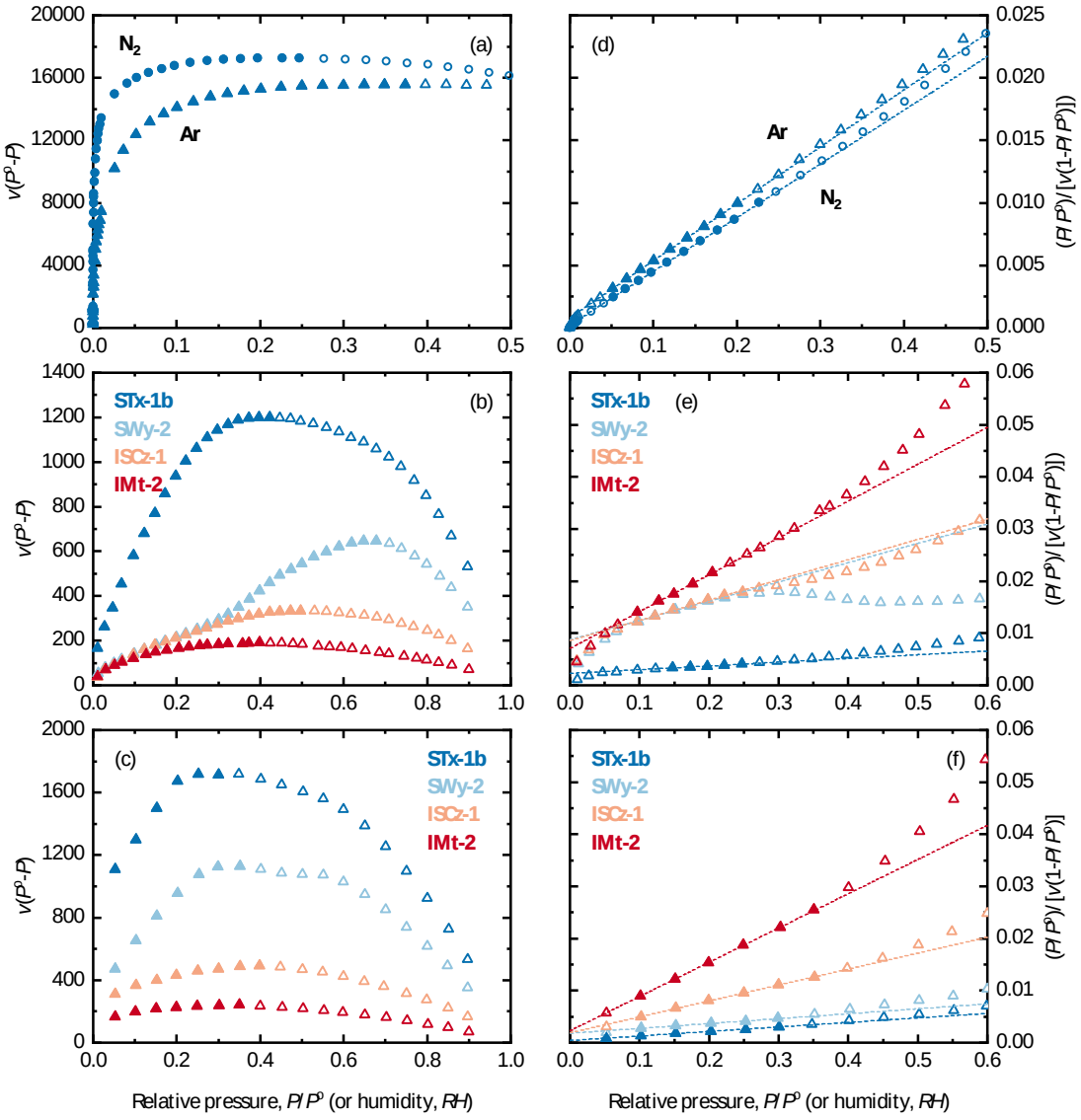

Figure S5: $v(P^{o} - P)$ plotted (a) against P/P^{o} for N_2 and Ar on STx-1b, and (b) against RH for water (a) adsorption and (b) desorption isotherms. The closed symbols are the data points for which $v(P^{o} - P)$ increases monotonically as a function of P/P^{o} or RH. The points below the maximum value of $v(P^{o} - P)$ were considered for the BET calculation according to the Rouquerol method.[S7] The linearized form of the BET equation is plotted for (d) N_2 and Ar on STx-1b, and water (e) adsorption and (f) desorption isotherms where the points (closed symbols) are used to estimate S_{BET}. The dashed lines are linear regression fits.

where N_A is the Avogadro's number, σ is the cross sectional molecular area, and $v_{m,STP}$ is the adsorbate molar volume at the STP condition (22.4 L/mol). The linear region of the BET plot was determined using the criteria suggested by the Rouquerol method.[S7] The values of σ for N_2, Ar, and water are 0.162 nm^2, 0.142 nm^2 and 0.125 nm^2, respectively. As discussed in the main manuscript, the linear regions are more clearly defined for the desorption isotherms of water as shown in Figure S5e and f, and the values of P/P^o at v_m are outside the P/P^o range used to determine the surface area. Table S2 summarizes the BET parameters.

Table S2: BET parameters obtained from water adsorption and desorption isotherms

Parameter		STx-1b	SWy-2	ISCz-1	IMt-2
Adsorption	v_m [cm^3/g STP]	105.9	22.75	21.08	12.85
	C	4.13	5.86	5.52	11.0
	P/P^o range	0.15–0.25	0.10–0.22	0.10–0.25	0.10–0.21
	P/P^o at v_m	0.36	0.27	0.28	0.23
	R^2	0.998	0.991	0.993	0.999
Desorption	v_m [cm^3/g STP]	109.9	91.53	30.78	14.70
	C	21.6	6.24	17.0	29.5
	P/P^o range	0.05–0.3	0.10–0.3	0.10–0.35	0.10–0.35
	P/P^o at v_m	0.18	0.29	0.20	0.16
	R^2	0.995	0.996	0.999	1

The internal surface areas, S_{int}, of the swelling clay minerals (STx-1b, SWy-2, and ISCz-1) have been calculated using the method proposed by Mooney et al.[S8]: $S_{int} = 2(S_{BET,w} - S_{ext})$ where S_{ext} is the external surface area assumed to be S_{BET} of N_2 or Ar. The values from Ar measurements were used in this study. Table S3 summarizes the values of S_{int} for STx-1b, SWy-2, and ISCz-1.

Table S3: Internal surface area of smectite clay minerals

Surface area	Unit	STx-1b	SWy-2	ISCz-1
$S_{BET,w}$	[m^2/g]	366.21 ± 2.95	303.51 ± 3.89	101.95 ± 1.41
$S_{ext,Ar}$	[m^2/g]	82.31 ± 0.10	33.14 ± 0.21	30.15 ± 0.16
S_{int}	[m^2/g]	567.80 ± 5.90	540.75 ± 7.78	143.59 ± 2.84

He Gravimetry

The skeletal volume of the sample and suspended metal parts, V_0, was measured by introducing He into the measuring chamber under the assumption that the adsorption of He is negligibly small making the left-hand side of Equation 1 of the main manuscript equal to zero:

$$\mathrm{MP}_1(\rho, T) - \mathrm{MP}_{1,0} = -\rho_{\mathrm{He}} V_0 \tag{5}$$

The negative value of the slope of the linear fit to a plot of $\mathrm{MP}_1 - \mathrm{MP}_{1,0}$ against ρ_{He} is equal to V_0. The bulk density of He, ρ_{He}, was calculated *in situ* from the buoyancy exerted on a titanium sinker with a known volume ($V_{\mathrm{sk}} = 4.364 \pm 0.002$ cm^3) using the following equation:

$$\rho_{\mathrm{He}} = \frac{\left(\mathrm{MP}_{2,0} - \mathrm{MP}_{1,0}\right) - \left(\mathrm{MP}_2(\rho, T) - \mathrm{MP}_1(\rho, T)\right)}{V_{\mathrm{sk}}} \tag{6}$$

where $\mathrm{MP}_2(\rho, T)$ are the combined weights of $\mathrm{MP}_1(\rho, T)$ and the titanium sinker, and $\mathrm{MP}_{2,0}$ is the same measured under vacuum. The procedure was equally applied to the hydrated samples to obtain the volume that also included the pre-adsorbed water volume, $V_0 + V_{\mathrm{w}}$. As

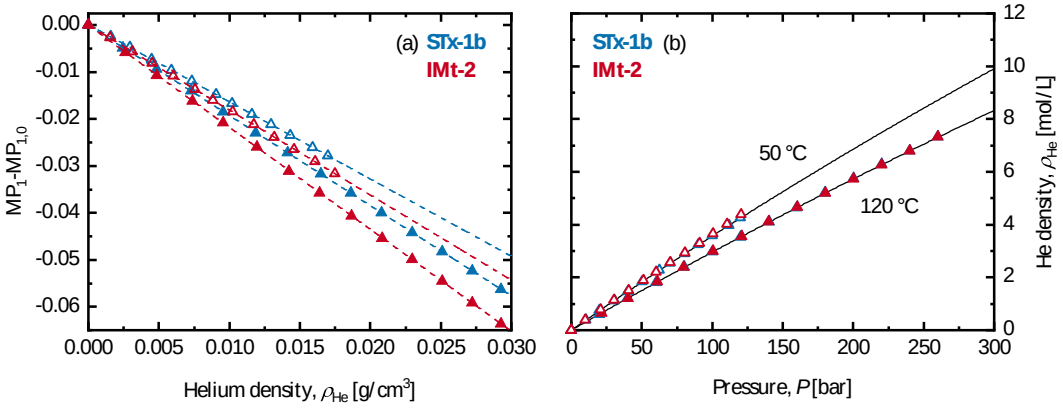

Figure S6: (a) Normalized measured weight plotted against He bulk density for dry STx-1b and IMt-2 (closed symbols) at 120 °C and hydrated STx-1b and IMt-2 (open symbols) at 50 °C. (b) He bulk density measured *in situ* compared to the calculated values obtained from Lemmon et al.[S9].

shown in Figure S6, the He gravimetric measurements were performed at 50 °C (from vacuum

to 120 bar in 10 bar increments) for the hydrated samples as to not excessively dehydrate the samples while the measurements on the dry samples were carried out at 120 °C (from vacuum to 260 bar in 20 bar increments) to minimize the amount of possible He adsorption.

Thermogravimetric Analysis

The thermogravimetric analysis (TGA) was performed using TGA Q500 (TA Instruments) up to 1000 °C heated at a rate of 10 °C/min after equilibrating at 30 °C. The sample atmosphere was purged with N_2 gas with a purge rate of 60 mL/min. Figure S7 shows the weight loss from the initial weight for the four source clay minerals as well as the derivative weight change with respect to temperature.

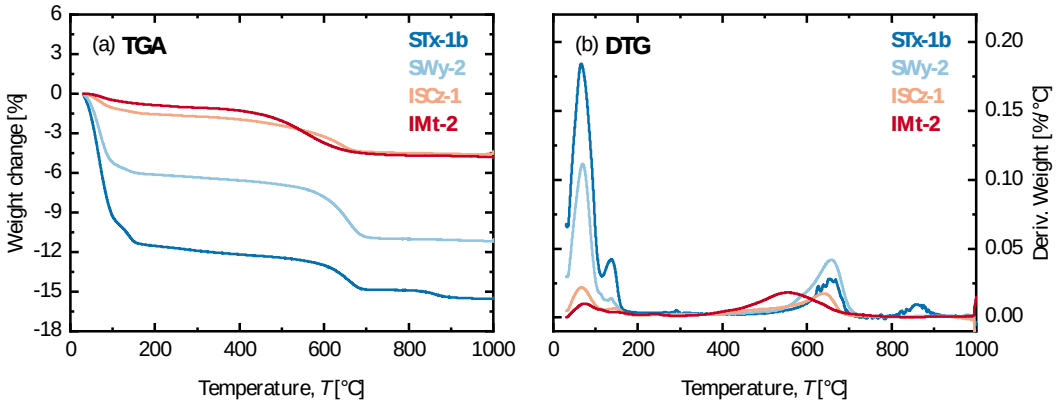

Figure S7: (a) TGA curves and (b) DTG curves that show two distinct regions of significant weight loss for all four clay minerals: one below 200 °C and another at approximately between 500 °C to 700 °C.

X-ray Diffraction Analysis

The X-ray diffraction (XRD) patterns were collected using X'Pert Pro from PANalytical equipped with a copper anode ($\lambda = 1.54$ Å). The measurements were collected from 2θ of 5° to 60° with a scan step size of 0.03°. The values of d_{001} spacing were calculated using the Bragg's Law.

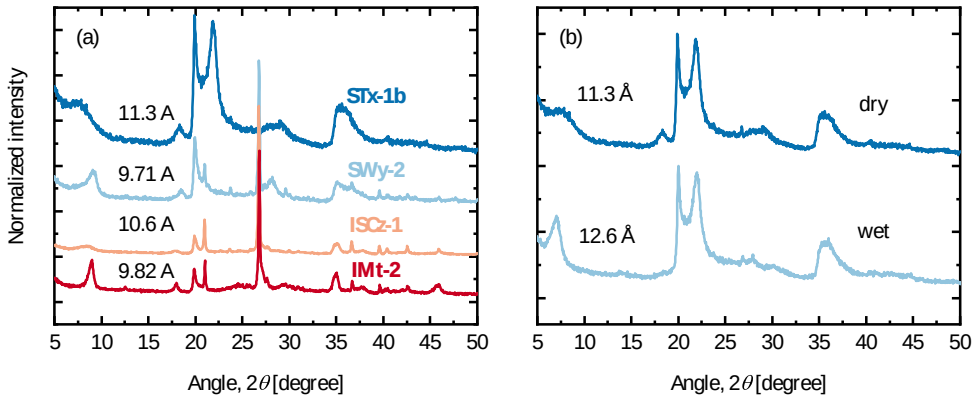

Figure S8: (a) XRD patterns of the four clay minerals after being completely dried at 200 °C and (b) XRD patterns of dry and hydrated STx-1b with d_{001} spacing.

Modeling Methodology

Lattice Density Functional Theory

The equations of the Lattice Density Functional Theory (LDFT) have been described in detail in our previous work.[S10,S11] The values of the saturation factor, c_{sat}, calculated in this work agree well with the linear correlation reported in Hwang and Pini[S11] ($c_{\text{sat}} = 1.07(T_{\text{c}}/T) - 0.07$) as shown in Figure S9.

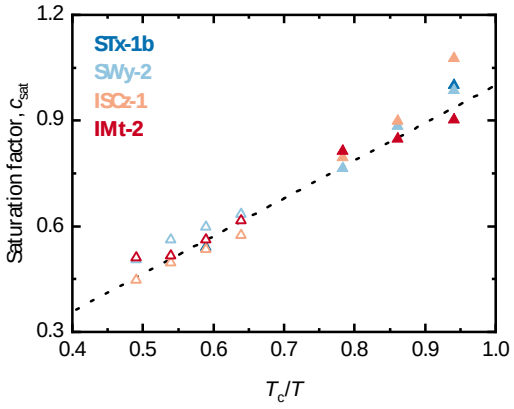

Figure S9: Saturation factors of CO_2 (closed symbols) and CH_4 (open symbols) as a function of T_{c}/T.

Pore-Size Distributions

The pore size distributions (PSD) were obtained from Ar adsorption isotherms using the non-local density functional theory (NLDFT) on zeolite cylindrical model (fitting error of 0.406 %). The micropore volumes were obtained from the CO_2 adsorption isotherms using the grand canonical Monte Carlo (GCMC) on carbon model (fitting error of 3.807 %). Figure S10 shows the fitting comparisons between the models and experimental isotherms, and the corresponding PSDs and their discretization.

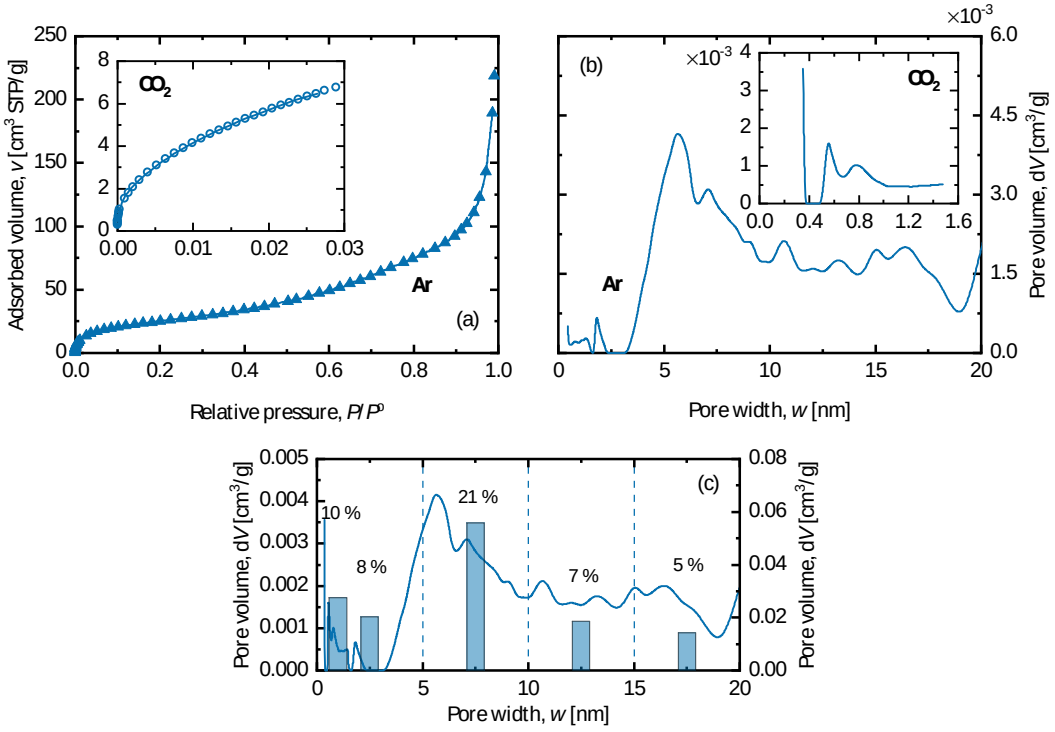

Figure S10: (a) Ar and CO_2 (inset) adsorption isotherms on STx-1b (symbols) with the respective NLDFT and GCMC fits (solid lines). (b) Pore volume distributions of STx-1b obtained from Ar (up to 20 nm) and CO_2 (inset) using the aforementioned models. (c) Discretization of the combined pore volume distributions (solid line) obtained from Ar and CO_2 adsorption isotherms. The volumes of the discretized lattice pores (bars) are linked to the right y-axis and their respective pore volume percentages are labeled.

High-Pressure Sorption Data

Table S4, S5, S6, and S7 summarize the sorption data on dry STx-1b and IMt-2. Table S8, S9, S10, and S11 summarize the sorption data on hydrated STx-1b and IMt-2.

Table S4: Measured excess amount of CO_2 on dry STx-1b at 50 °C

P [bar]	Density [mol/L]	n^{ex} [mmol/g]	Error [mmol/g]
0.21	0.009	0.059	0.001
0.51	0.020	0.089	0.001
1.02	0.039	0.125	0.001
3.02	0.114	0.222	0.001
6.01	0.229	0.315	0.001
10.02	0.388	0.411	0.001
17.03	0.679	0.539	0.001
24.98	1.032	0.654	0.002
34.02	1.476	0.765	0.002
44.14	2.024	0.874	0.003
57.01	2.847	0.992	0.003
67.93	3.701	1.078	0.004
82.15	5.218	1.158	0.006
95.09	7.368	1.121	0.009
105.09	9.846	0.944	0.011
120.11	13.047	0.664	0.015
135.11	14.717	0.535	0.019
175.20	16.942	0.394	0.020
230.11	18.483	0.317	0.021
274.98	19.320	0.280	0.022
112.47	11.673	0.787	0.013
90.01	6.383	1.164	0.010
14.05	0.552	0.516	0.001

Table S5: Measured excess amount of CH_4 on dry STx-1b at 50 °C

P [bar]	Density [mol/L]	n^{ex} [mmol/g]	Error [mmol/g]
0.21	0.008	0.009	0.002
0.48	0.018	0.014	0.002
1.01	0.038	0.022	0.002
3.01	0.112	0.048	0.002
6.02	0.226	0.078	0.002
10.03	0.378	0.110	0.002
14.99	0.568	0.144	0.002
21.00	0.802	0.178	0.002
30.01	1.159	0.221	0.003
42.87	1.685	0.270	0.003
60.18	2.409	0.318	0.004
80.18	3.274	0.356	0.004
110.52	4.620	0.384	0.006
145.58	6.182	0.386	0.008
189.81	8.058	0.362	0.010
239.08	9.902	0.321	0.012
295.71	11.664	0.274	0.014
100.05	4.149	0.380	0.005
59.79	2.390	0.324	0.004
16.98	0.643	0.165	0.003
7.97	0.299	0.105	0.002
1.98	0.074	0.048	0.002

Table S6: Measured excess amount of CO_2 on dry IMt-2 at 50 °C

P [bar]	Density [mol/L]	n^{ex} [mmol/g]	Error [mmol/g]
0.50	0.020	0.031	0.001
1.61	0.061	0.052	0.001
3.05	0.116	0.072	0.001
6.01	0.229	0.099	0.001
10.03	0.388	0.125	0.001
17.04	0.678	0.159	0.001
25.00	1.032	0.188	0.001
34.00	1.474	0.213	0.001
44.10	2.022	0.233	0.002
56.25	2.792	0.251	0.002
67.68	3.680	0.263	0.003
79.98	4.936	0.266	0.004
95.11	7.361	0.232	0.006
120.51	13.095	0.098	0.010
109.94	11.077	0.143	0.008
86.21	5.773	0.263	0.004
50.00	2.372	0.256	0.002
30.04	1.270	0.220	0.001
10.03	0.388	0.144	0.001
4.96	0.188	0.108	0.001

Table S7: Measured excess amount of CH_4 on dry IMt-2 at 50 °C

P [bar]	Density [mol/L]	n^{ex} [mmol/g]	Error [mmol/g]
0.54	0.022	0.015	0.002
1.54	0.060	0.018	0.002
3.03	0.115	0.023	0.002
6.05	0.229	0.030	0.002
10.02	0.380	0.039	0.002
20.07	0.767	0.055	0.002
30.23	1.169	0.067	0.002
39.90	1.565	0.074	0.002
50.56	2.005	0.081	0.002
60.62	2.429	0.084	0.002
80.53	3.289	0.087	0.003
100.80	4.187	0.087	0.003
120.15	5.053	0.083	0.004
149.82	6.369	0.074	0.005
107.78	4.495	0.088	0.004
89.55	3.683	0.090	0.003
50.14	1.985	0.082	0.002
29.95	1.156	0.067	0.002
9.49	0.358	0.038	0.002
4.95	0.185	0.026	0.002

Table S8: Measured excess amount of CO_2 on hydrated STx-1b at 50 °C

P [bar]	Density [mol/L]	n^{ex} [mmol/g]	Error [mmol/g]
5.02	0.188	0.538	0.002
10.04	0.386	0.718	0.002
20.12	0.809	0.937	0.003
29.98	1.265	1.085	0.003
39.79	1.774	1.198	0.004
60.15	3.068	1.376	0.008
83.43	5.383	1.480	0.010
90.60	6.470	1.450	0.011
100.41	8.595	1.321	0.015
110.00	11.077	1.098	0.019
119.68	12.983	0.924	0.029

Table S9: Measured excess amount of CH_4 on hydrated STx-1b at 50 °C

P [bar]	Density [mol/L]	n^{ex} [mmol/g]	Error [mmol/g]
5.39	0.210	0.183	0.005
10.22	0.394	0.238	0.004
20.16	0.778	0.310	0.005
30.26	1.179	0.366	0.005
43.84	1.734	0.423	0.006
60.19	2.419	0.473	0.006
81.72	3.349	0.507	0.007
101.49	4.227	0.536	0.008
120.18	5.064	0.548	0.009
139.94	5.943	0.551	0.011
168.74	7.191	0.534	0.013

Table S10: Measured excess amount of CO_2 on hydrated IMt-2 at 50 °C

P [bar]	Density [mol/L]	n^{ex} [mmol/g]	Error [mmol/g]
5.00	0.189	0.091	0.001
19.99	0.806	0.172	0.001
40.24	1.803	0.220	0.003
60.19	3.072	0.244	0.003
81.22	5.095	0.240	0.006
100.31	8.565	0.174	0.011
120.44	13.083	0.062	0.014

Table S11: Measured excess amount of CH_4 on hydrated IMt-2 at 50 °C

P [bar]	Density [mol/L]	n^{ex} [mmol/g]	Error [mmol/g]
5.17	0.194	0.024	0.003
20.39	0.779	0.056	0.003
40.75	1.597	0.075	0.004
60.53	2.423	0.085	0.004
81.27	3.320	0.092	0.005
100.58	4.175	0.091	0.006
120.36	5.061	0.088	0.007
170.71	7.266	0.069	0.010

References

(S1) Bérend, I.; Cases, J.-M.; Francois, M.; Uriot, J.-P.; Michot, L.; Masion, A.; Thomas, F. Mechanism of Adsorption and Desorption of Water Vapor by Homoionic Montmorillonites: 2. The Li^+, Na^+, K^+, Rb^+, and Cs^+-Exchanged Forms. *Clays and Clay Minerals* **1995**, *43*, 324–336.

(S2) Cases, J.-M.; Berend, I.; Francois, M.; Uriot, J. P.; Michot, L. J.; Thomas, F. Mechanism of adsorption and desorption of water vapor by homoionic montmorillonite: 3. The Mg^{2+}, Ca^{2+}, Sr^{2+} and Ba^{2+} exchanged form. *Clays and Clay Minerals* **1997**, *45*, 8–22.

(S3) Xu, W.; Johnston, C. T.; Parker, P.; Agnew, S. F. Infrared Study of Water Sorption on Na-, Li-, Ca-, and Mg-Exchanged (SWy-1 and SAz-1) Montmorillonite. *Clays and Clay Minerals* **2000**, *48*, 120–131.

(S4) Cases, J.-M.; Berend, I.; Besson, G.; Francois, M.; Uriot, J. P.; Thomas, F.; Poirier, J. E. Mechanism of adsorption and desorption of water vapor by homoionic montmorillonite. 1. The sodium-exchanged form. *Langmuir* **1992**, *8*, 2730–2739.

(S5) Thommes, M.; Kaneko, K.; Neimark, A. V.; Olivier, J. P.; Rodriguez-Reinoso, F.; Rouquerol, J.; Sing, K. S. W. Physisorption of gases, with special reference to the evaluation of surface area and pore size distribution (IUPAC Technical Report). *Pure and Applied Chemistry* **2015**, *87*, 1051–1069.

(S6) Brunauer, S.; Emmett, P. H.; Teller, E. Adsorption of Gases in Multimolecular Layers. *Journal of the American Chemical Society* **1938**, *60*, 309–319.

(S7) Rouquerol, F.; Rouquerol, J.; Sing, K. S. W.; Llewellyn, P.; Maurin, G. *Adsorption by Powders and Porous Solids: Principles, Methodology and Applications*, 2nd ed.; Academic Press: Oxford, 2014.

(S8) Mooney, R. W.; Keenan, A. G.; Wood, L. A. Adsorption of Water Vapor by Montmorillonite. II. Effect of Exchangeable Ions and Lattice Swelling as Measured by X-Ray Diffraction. *Journal of the American Chemical Society* **1952**, *74*, 1371–1374.

(S9) Lemmon, E. W.; Bell, I. H.; Huber, M. L.; McLinden, M. O. NIST Standard Reference Database 23: Reference Fluid Thermodynamic and Transport Properties-REFPROP. 2018; `https://www.nist.gov/srd/refprop`.

(S10) Hwang, J.; Joss, L.; Pini, R. Measuring and modelling supercritical adsorption of CO_2 and CH_4 on montmorillonite source clay. *Microporous and Mesoporous Materials* **2019**, *273*, 107–121.

(S11) Hwang, J.; Pini, R. Supercritical CO_2 and CH_4 Uptake by Illite-Smectite Clay Minerals. *Environmental Science and Technology* **2019**, *53*, 11588–11596.